FOSSIL ENERGY

DOE/BC/15211-17
(OSTI ID: 792462)

NON-ADIABATIC EFFECTS ON COMBUSTION FRONT PROPAGATION IN POROUS MEDIA: MULTIPLICITY OF STEADY STATES

Topical Report
October 2001

By
I. Yücel Akkutlu
Yanis C. Yortsos

Date Published: March 2002

Work Performed Under Contract No. DE-AC26-99BC15211

University of Southern California
Los Angeles, California

National Energy Technology Laboratory
National Petroleum Technology Office
U.S. DEPARTMENT OF ENERGY
Tulsa, Oklahoma

DOE/BC/15211-17
Distribution Category UC-122

Non-Adiabatic Effects on Combustion Front Propagation in Porous Media: Multiplicity of Steady States

By
I. Yücel Akkutlu
Yanis C. Yortsos

March 2002

Work Performed Under DE-AC26-99BC15211

Prepared for
U.S. Department of Energy
Assistant Secretary for Fossil Energy

Tom Reid, Project Manager
National Petroleum Technology Office
P.O. Box 3628
Tulsa, OK 74101

Prepared by
Department of Chemical Engineering
University of Southern California
University Park Campus
HEDCO 316, USC
Los Angeles, CA 90089-1211

TABLE OF CONTENTS

Abstract

The sustained propagation of combustion fronts in porous media is a necessary condition for the success of an *in situ* combustion project for oil recovery. Compared to other recovery methods, in situ combustion involves the added complexity of exothermic reactions and temperature-dependent chemical kinetics. In the presence of heat losses, the possibility of ignition and extinction (quenching) exists. In this report, we address the properties of combustion fronts propagating at a constant velocity in the presence of heat losses.

We describe an analytical method for solving this problem by treating the reaction region as a discontinuity. Using a rigorous perturbation approach, similar to that used in the smoldering combustion [3] and the propagation of flames [6], we derive appropriate jump conditions that relate the change in dependent variables across the front. These conditions account for the kinetics of the reaction between oxygen and fuel, and the heat and mass transfer in the reaction zone. Then, the problem reduces to the modeling of the dynamics of a combustion front, on either side of which transport of heat and mass, but not chemical reactions, must be considered. Properties of the two regions are coupled using the jump conditions.

Expressions for temperature and velocity of the combustion front, concentration of oxygen left unreacted, as well as spatial profiles for temperature and concentrations are obtained under both adiabatic and non-adiabatic conditions. The heat losses to the surrounding are incorporated to the energy balance using two different modes (1) a linear convective term in terms of an overall heat transfer coefficient, and (2) a conductive integral term, which allows for heat transfer by vertical conduction to the surrounding porous medium. The sensitivity of the variables to parameters, such as the injection rate and air content is analyzed.

The combustion front in the presence of heat losses to the surrounding behaves markedly different than an adiabatic one. We observe the existence of multiple steady-state solutions with stable low and high temperature branches, and an unstable intermediate branch. Conditions for a self-sustaining front propagation are investigated as a function of injection and reservoir properties. A critical extinction threshold exists and is expressed in terms of the system properties. For fixed inlet conditions, the thickness of the reservoir, the heat capacity of solid, heat of reaction, the initially available fuel concentration, and the reaction activation energy are the most influential reservoir parameters. Using the expressions obtained with the two non-adiabatic models an explicit formulation is obtained for the overall heat transfer coefficient in terms of reservoir thickness and front velocity. The coefficient is observed to be not only dependent on the thermal properties of the porous medium but also to the front dynamics.

1 INTRODUCTION

The propagation of combustion fronts in porous media is a subject of interest to a variety of applications, ranging from the *in situ* combustion for the recovery of oil [1] to filtration and smoldering combustion [2], [3]. While these problems may differ in application and context, they share the common characteristic that the combustion reaction involves the burning of a stationary solid fuel. The fuel may pre-exist or it may be created by the processes preceding the combustion reaction, such as vaporization and low temperature oxidation. *In situ* combustion for oil recovery has been studied extensively since the mid 1950s. The texts by Prats [1] and Boberg [4] summarize the relevant literature on the subject until the late 1980s. A large number of experimental, analytical and numerical studies have been reported.

The dynamics of the combustion front are influenced by a number of factors, including the fluid flow of injected and produced gases, the heat transfer in the porous medium and the surroundings, the rate of reaction(s), the heterogeneity of the medium and possibly the evolution of the pore morphology due to the combustion reaction. Understanding these dynamics is important to front stability, the sustained propagation of combustion, the effects of heterogeneity, and the scale-up of the process. Because of the very thin reaction zone, associated with typical combustion, conventional numerical models used for this purpose may not be adequate, however, and a more detailed description is necessary. This is particularly the case for process scale-up, which is the averaging over larger scales, such as the reservoir grid simulation scale. Upscaling is necessary for a realistic description of flow and transport in heterogeneous subsurface formations and it is a subject of great interest [5]. The presence of frontal discontinuities, expected in combustion fronts, adds a novel and important feature to the upscaling of combustion processes.

Combustion fronts have been studied extensively in the literature of combustion and flames. Among the great deal of articles published we refer to earlier works by Matalon and Matkowsky [6], the monograph of Pelcé [7] and the more recent work of Schult and co-workers [3]. Ref. [6] discusses the propagation of flames in the combustion of premixed gases, in the absence of a porous medium, and treats the flame front as a discontinuity, separating two regions of dif-

ferent temperature and chemical composition. The reaction zone is analyzed using methods of singular perturbation. Pelcé [7] presents an interesting compilation of studies on combustion and flame propagation in a variety of geometries. He shows that common aspects exist between the seemingly different problems of viscous displacements in a Hele-Shaw cell (which gives rise to viscous fingering in porous media), dendritic solidification and flame propagation.

By comparison, relatively few studies exist in the literature of *in situ* combustion. Baily and Larkin [8] provided simple heat transfer models in linear and radial geometries in the presence of a combustion zone of finite thickness. Gottfried [9] treated the combustion front as a discontinuity involving a point heat source, but without exploring the combustion zone structure. Beckers and Harmsen [10] detailed the propagation of various regimes in *in situ* combustion and its variants, e.g. wet combustion. Burger and Sahuquet [11] analyzed the chemical aspects of the reaction processes. Ağca and Yortsos [12] proposed a simplified description, which takes into account the heat losses to the surroundings and discuss sustained propagation and extinction. Their analysis is based on a steadily propagating combustion front, but with an *a priori* known thickness, however. The stability of combustion fronts was analyzed by Armento and Miller [13].

In a series of recent papers, Schult et al. [3, 14] studied the adiabatic combustion of a homogeneous porous medium. This problem, known as filtration combustion, appears in various applications. They provided an asymptotic analysis in 1-D following an approach similar to the flame analysis of Ref. [6]. A somewhat analogous approach was attempted earlier by Britten and Krantz [15, 16] who examined the structure of the reaction zone in reverse combustion in the context of coal gasification.

The objective of this work is to apply a similar approach but in the context of *in situ* combustion. Because many aspects are common between the two processes, one can exploit profitably the advances made in filtration combustion, as will be shown below. However, there are also several differences. For example, in filtration combustion, (1) the fuel is *a priori* available, rather than in-situ generated; (2) phenomena preceding the combustion front are unimportant; (3) the heterogeneity of the porous medium is generally weak; while, (4) effects of heat losses are not included. Addressing these differences is necessary and

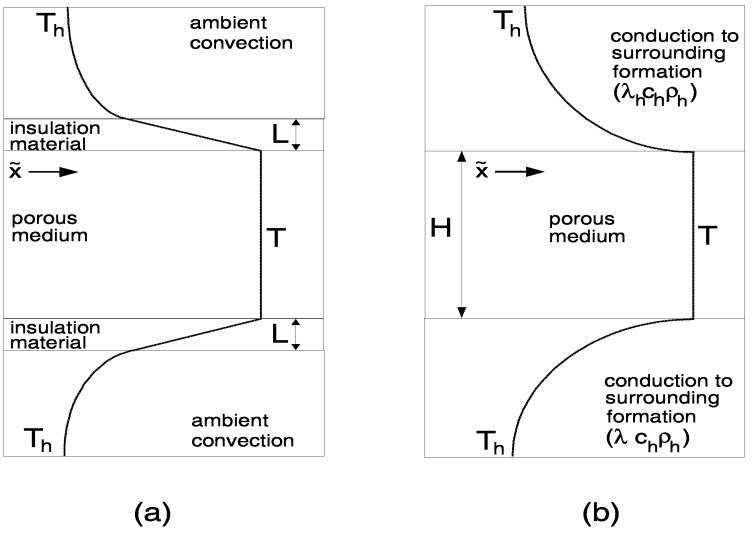

Figure 1: Representation of heat losses to the surrounding during *in situ* combustion process with (a) convective and (b) conductive modes.

requires a multi-faceted investigation. In the present report, we will specifically consider only the last of the above aspects, namely the effect of heat losses. These we will model by two different modes, a convective and a conductive mode. The first is more applicable to laboratory-type processes (Fig. 1a). The second involves heat conduction in the practically semi-infinite strata bounding the reservoir, where in-situ combustion takes place (Fig. 1b). It is more appropriate for a subsurface process. For either, we will focus on the effect on the sustained propagation/extinction properties of combustion fronts. Because our emphasis is on non-adiabatic effects, we will proceed with the 1-D analysis of [3] and neglect for the present purposes the other effects mentioned above, including heterogeneity and phenomena preceding the combustion front, which are to be studied in a separate investigation.

The report is organized as follows: First, we briefly describe some general aspects of *in situ* combustion. The asymptotic framework of [3] is next applied to the propagation of reaction fronts. The results are used to analyze non-adiabatic heat transfer in the adjacent combustion zone. Subsequently, we consider 1-D moving fronts of constant velocity and present a sensitivity study of the effect of the various parameters, with emphasis on extinction, ignition and sustained propagation. The model used is a continuum, in which effective values are used for kinetic and transport parameters. A parallel study [17] addresses the same

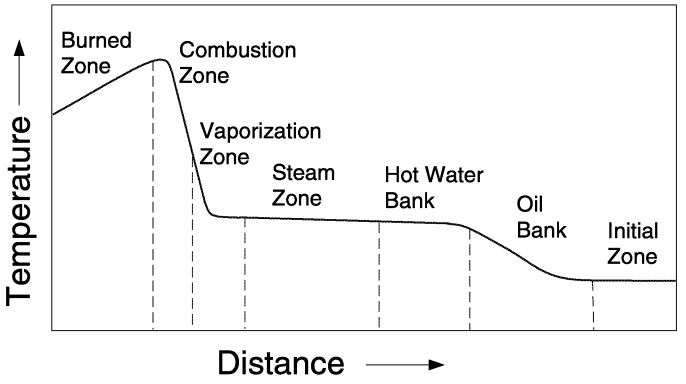

Figure 2: Characteristic regions of *in situ* combustion process.

process, but using a discrete pore-network model.

2 PRELIMINARIES

In *in situ* combustion, one can generally identify the following regions [1]: (1) a burned zone, (2) a combustion zone, (3) a vaporization zone, (4) a steam (condensation) zone, (5) a hot water bank, (6) an oil bank and (7) an initial zone (see schematic of Figure 2).

The burned zone contains injected air and possibly a residue of unburned fuel depending on the combustion efficiency. The temperature in this region increases monotonically downstream, until the combustion zone. In this zone, solid fuel and injected oxygen react exothermically to generate combustion gases, such as carbon oxides and superheated steam. In the vaporization zone, fluid hydrocarbons are vaporized, thermally cracked, distilled by the flowing gas stream and decarboxylated.

The combustion reactions of hydrocarbon mixtures are complex: a great number of reaction products are generated by hydrocarbon oxidation over a large temperature range [11]. It is not uncommon to classify these groups into two lumped-parameter, single-step reactions: high temperature oxidation (HTO) and low temperature oxidation (LTO), with HTO occuring in the combustion zone. LTO processes are partly responsible for fuel generation. Fuel combustion in the HTO region is often generalized as an oxidation reaction with a

large activation energy. The combustion stoichiometry is typically represented by the simple exothermic reaction [18]

$$CH_x + \left(1 - \frac{m}{2} + \frac{x}{4}\right) O_2 \longrightarrow (1-m)CO_2 + mCO + \frac{x}{2}H_2O \tag{1}$$

where x is the fuel atomic H-C ratio and m the fraction of carbon oxidized to CO. For the purposes of this report, we will adopt the notation of [3] and write

[Fuel] + $\tilde{\gamma}$ [Oxygen] $\longrightarrow \tilde{\gamma}_{gp}$ [Gaseous Product]

where $\tilde{\gamma}_i$ are stoichiometric coefficients. In the above, we have used pseudo-components for the fuel and the reaction products.

Unreacted or bypassed oxygen reacts with the hydrocarbons ahead of the combustion front where the temperature is lower. In this region, LTO tends to increase the density, apparent viscosity and boiling range of the liquid phase oil. Clearly fuel formation and combustion are inter-dependent. Excessive fuel deposition may retard the rate of advance of the combustion front, while insufficient fuel deposition may not provide enough heat supply to sustain it. As mentioned above, in this report we will assume a constant amount of available fuel, independent of the process in the combustion zone. Although perhaps questionable, this assumption is necessary to first understand the simpler problem of non-adiabatic combustion with a fixed fuel content. Then, the steady-state dynamics can be analyzed separately, assuming given values of fuel concentration and other properties downstream.

The vaporization zone is preceded by a steam zone, where generated steam condenses, and further ahead by a hot water bank, which displaces liquid oil (oil bank). The dynamics of these processes are all coupled to the combustion front. Attempts have recently been made to describe the propagation of such fronts using concepts from wave propagation [19].

3 FORMULATION

In formulating the conservation equations we make, in addition to the conventional, the following assumptions: pore space and solid matrix are in thermal equilibrium and a one-temperature model is used for the energy balance; heat transfer by radiation, energy source terms due to pressure increase, and work from surface and body forces are all negligible; the ideal gas law is the equation of state for the gas phase; thermodynamic and transport properties, such as conductivity, diffusivity, heat capacity of the solid, heat of reaction, etc. all remain constant.

In the following, we assume a 1-D geometry, of the type shown in Fig. 1. Conservation equations are written for the total energy, the oxygen mass, the total gas mass and the fuel mass. For the latter, we introduce the extent of conversion depth, $\eta(\tilde{x},\tilde{t}\,) = 1 - \rho_f(\tilde{x},\tilde{t})/\rho_f^o$, such that $\eta = 0$ corresponds to the initial state and $\eta = 1$ to complete consumption. The dependent variables are the temperature, $\tilde{T}(\tilde{x},\tilde{t}\,)$, the oxygen mass fraction, $\tilde{Y}(\tilde{x},\tilde{t}\,)$, the average gas density, $\rho_g(\tilde{T},\tilde{p})$, and the fuel conversion depth. We use Darcy's law for gas flow in the porous medium. The dimensional form of the equations (superscript tilde) is similar to [3] and reads as follows:

$$(1-\phi)c_s\rho_s\frac{\partial\tilde{T}}{\partial\tilde{t}} + c_g\rho_g\tilde{v}\frac{\partial\tilde{T}}{\partial\tilde{x}} = \lambda\frac{\partial^2\tilde{T}}{\partial\tilde{x}^2} + \tilde{Q}\rho_f^o W - \dot{Q}_h, \tag{2}$$

$$\phi\frac{\partial(\tilde{Y}\rho_g)}{\partial\tilde{t}} + \frac{\partial(\tilde{Y}\rho_g\tilde{v})}{\partial\tilde{x}} = D_M\frac{\partial}{\partial\tilde{x}}\left(\rho_g\frac{\partial\tilde{Y}}{\partial\tilde{x}}\right) - \tilde{\mu}\rho_f^o W, \tag{3}$$

$$\phi\frac{\partial\rho_g}{\partial\tilde{t}} + \frac{\partial}{\partial\tilde{x}}\left(\rho_g\tilde{v}\right) = \tilde{\mu}_g\rho_f^o W, \tag{4}$$

and

$$\frac{\partial\eta}{\partial\tilde{t}} = W, \tag{5}$$

where, $\dot{Q}_h$ is the heat loss term and W the rate of reaction. In the above, c_i denotes the average specific heat capacity of species i (gas or solid) at constant pressure, ρ_i is the volumetric

density of species i, and we assumed that the solid heat capacity is much larger than that of the gas. $\dot{Q}$ is the heat of combustion, D_M is an effective diffusion coefficient in the gas phase, while $\tilde{\mu} = \tilde{\gamma} M_o/M_f$ and $\tilde{\mu}_{gp} = \tilde{\gamma}_{gp} M_{gp}/M_f$ are mass-weighted stoichiometric coefficients for oxygen and gaseous products, respectively. The net gas mass production is determined by $\tilde{\mu}_g = \tilde{\mu}_{gp} - \tilde{\mu}$, so that $\tilde{\mu}_g > 0$ or $\tilde{\mu}_g < 0$ corresponds to gas mass production or consumption, respectively.For the rate of reaction, we use the law of mass action

$$W = k(\tilde{T}) \tilde{a}_s^m (\frac{\tilde{Y}\tilde{p}}{R\tilde{T}})^n \psi(\eta) \tag{6}$$

where

$$k(\tilde{T}) = k_o e^{-E/R\tilde{T}} \tag{7}$$

E is the activation energy and k_o the pre-exponential factor. The dependence on η is through the dimensionless function $\psi(\eta)$, the evaluation of which requires a more elaborate pore-level study [17]. Clearly, $\psi(1) = 0$. The rate is implicitly dependent on porosity, through the specific surface area per unit volume, $\tilde{a}_s$. In the applications to follow, exponents m and n will be set equal to one. Finally, we have Darcy's law

$$\frac{\partial \tilde{p}}{\partial \tilde{x}} = -\frac{\eta_g}{K(\eta)} \tilde{v} \tag{8}$$

where $K(\eta)$ is the absolute permeability and η_g is the gas viscosity, and the equation of state, assuming ideal gases

$$\tilde{p} M_g = \rho_g R\tilde{T}. \tag{9}$$

The expression for the heat losses takes two different forms. For a convective heat loss mode (Fig. 1a), we take a linear expression (Newton's law of cooling),

$$\dot{Q}_h = \frac{\tilde{h}}{H}(\tilde{T} - \tilde{T}_o) \tag{10}$$

where we introduced the overall heat transfer (film) coefficient, $\tilde{h}$. For a conductive heat loss mode (Fig. 1b) the expression is more elaborate [20]

$$\dot{Q}_h = \frac{2\sqrt{(\lambda_h c_h \rho_h)}}{H\sqrt{\pi}} \int_0^{\tilde{t}} \frac{\partial \tilde{T}}{\partial \tau} \frac{d\tau}{\sqrt{(\tilde{t}-\tau)}} \tag{11}$$

to reflect heat loss by conduction in the semi-infinite domain bounding the porous medium. Here H is the formation thickness and subscript h denotes surrounding properties.

4 SCALING AND NON-DIMENSIONALIZATION

The problem involves three spatial scales: the scale of the reaction zone, l_R, the scale of the combustion zone, l_T, and the convective scale, l_S. In the reaction zone, reaction and diffusion balance. The thickness of the reaction zone is of order Z^{-1} smaller than the combustion zone [3]

$$l_R \equiv \frac{l_T}{Z} \quad \text{where} \quad Z = \frac{E\tilde{T}_o}{R\tilde{T}_f^2} \tag{12}$$

Typically Z is large. As a result, and because the reaction rate is strongly temperature dependent, the combustion reactions are confined to a thin reaction-dominated zone at the combustion front. It is within this zone, where reactions occur at a high rate, temperature, pressure and concentrations being approximately constant. The reaction zone is embedded within the heat transfer layer, as shown in Figure 3. In the combustion zone, convection, conduction and heat losses balance, but reaction is negligible, and in the convection zone the dominant mode is convection. The reaction zone and the heat transfer layer combine to form the combustion zone (Figure 3). Outside this zone, the problem is controlled by convective transport of energy and mass, and also by heat losses to the surroundings.

Next, we introduce dimensionless space and time variables using the characteristic scales, $l^* = \frac{\alpha_s}{v_i}$ and $t^* = \frac{l^*}{v_i}$, where v_i is the injection velocity and α_s the effective thermal diffusivity. This notation is different from [3], although the subsequent analysis is similar. Scaling temperature

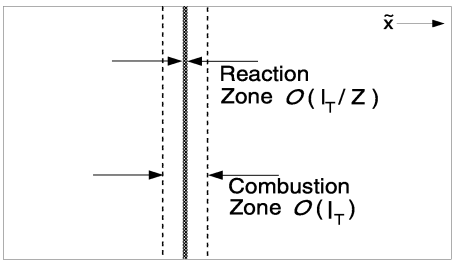

Figure 3: Schematics of reaction and combustion zones.

with $\tilde{T}_o$ and using the combustion zone formulation, we obtain the dimensionless conservation equations

$$\frac{\partial \theta}{\partial \hat{t}} + a\rho v \frac{\partial \theta}{\partial \hat{x}} = \frac{\partial^2 \theta}{\partial \hat{x}^2} + q\Phi - \dot{Q}_{hD} \tag{13}$$

$$\phi \frac{\partial (Y\rho)}{\partial \hat{t}} + \frac{\partial (Y\rho v)}{\partial \hat{x}} = \frac{1}{Le} \frac{\partial}{\partial \hat{x}} \left(\rho \frac{\partial Y}{\partial \hat{x}} \right) - \mu\Phi \tag{14}$$

$$\phi \frac{\partial \rho}{\partial \hat{t}} + \frac{\partial (\rho v)}{\partial \hat{x}} = \mu_g \Phi \tag{15}$$

and

$$\frac{\partial \eta}{\partial \hat{t}} = \Phi \tag{16}$$

where

$$\Phi = Z a_s \left(\frac{Y(1 + \Pi p)}{\theta} \right) \psi(\eta) \exp\left(Z\theta_f^2 \left(\frac{1}{\theta_f} - \frac{1}{\theta} \right) \right) \tag{17}$$

and in addition

$$\frac{\partial p}{\partial \hat{x}} = -\kappa v \qquad \text{and} \qquad \rho\theta = 1 + \Pi p. \tag{18}$$

In the above, we introduced the following variables and parameters

$$\begin{aligned}
\hat{x} &= \frac{\tilde{x}}{l^*}, \quad \hat{t} = \frac{\tilde{t}}{t^*}, \quad \theta = \frac{\tilde{T}}{\tilde{T}_o}, \qquad \theta_f = \frac{\tilde{T}_f}{\tilde{T}_o}, \qquad Y = \frac{\tilde{Y}}{Y_i}, \qquad p = \frac{\tilde{p} - \tilde{p}_i}{\tilde{p}_{inj} - \tilde{p}_i}, \qquad v = \frac{\tilde{v}}{v_i}, \\
\Pi &= \frac{\tilde{p}_{inj} - \tilde{p}_i}{\tilde{p}_i}, \qquad \mu = \frac{\tilde{\mu}\rho_f^o}{\rho_{gi} Y_i}, \qquad \mu_{pg} = \frac{\tilde{\mu}_{pg}\rho_f^o}{\rho_{gi} Y_i}, \qquad \mu_g = \frac{\tilde{\mu}_g \rho_f^o}{\rho_{gi}}, \qquad a = \frac{c_g \rho_{gi}}{(1-\phi) c_s \rho_s}, \\
q &= \frac{Q\rho_f^o}{(1-\phi) c_s \rho_s \tilde{T}_o}, \qquad \kappa = \frac{\eta_g x_* v_i}{K(\tilde{p}_{inj} - \tilde{p}_i)}, \qquad \Phi = Wt^*, \qquad \dot{Q}_{hD} = \frac{\dot{Q}_h t^*}{(1-\phi) c_s \rho_s \tilde{T}_o}, \\
\alpha_s &= \frac{\lambda}{(1-\phi) c_s \rho_s}, \qquad Le = \frac{\alpha_s}{D_M}
\end{aligned} \tag{19}$$

The boundary conditions depend on the extent of combustion. If the fuel is fully consumed (fuel-deficient case)

$$Y = 1, \qquad \theta = \theta_f, \qquad \eta = 1 \qquad ; \qquad \hat{x} \to -\infty \tag{20}$$

$$Y = Y_b, \qquad \theta = 1, \qquad \eta = 0 \qquad ; \qquad \hat{x} \to \infty \tag{21}$$

where θ_f and Y_b are to be determined. Here, a reaction-leading structure emerges, where the temperature profile and the high temperature region trail the combustion front. Otherwise,

$$Y = 1, \qquad \theta = 1, \qquad \eta = \eta_b \qquad ; \qquad \hat{x} \to -\infty \tag{22}$$

$$Y = 0, \qquad \theta = \theta_f, \qquad \eta = 0 \qquad ; \qquad \hat{x} \to \infty \tag{23}$$

where θ_f and η_b are to be determined. This is the oxygen-deficient case with the high temperature region located ahead of the front, thus yielding a reaction-trailing structure. However, only the reaction-leading case will be considered below.

The final step is to convert to coordinates moving with the combustion front, which in the fuel-deficient case can be defined, e.g. as the position at which $\eta = 1/2$. In the moving coordinates $\xi = \hat{x} - f(\hat{t})$, and $t = \hat{t}$, the non-dimensional equations take the form

$$\frac{\partial \theta}{\partial t} + (a\rho v - f_t) \frac{\partial \theta}{\partial \xi} = \frac{\partial^2 \theta}{\partial \xi^2} + q\Phi - \dot{Q}_{hD} \tag{24}$$

$$\phi\frac{\partial(Y\rho)}{\partial t}+\frac{\partial(Y\rho(v-\phi f_t))}{\partial\xi}=\frac{1}{Le}\frac{\partial}{\partial\xi}\left(\rho\frac{\partial Y}{\partial\xi}\right)-\mu\Phi \tag{25}$$

$$\phi\frac{\partial\rho}{\partial t}+\frac{\partial(\rho(v-\phi f_t))}{\partial\xi}=\mu_g\Phi \tag{26}$$

$$\frac{\partial\eta}{\partial t}-f_t\frac{\partial\eta}{\partial\xi}=\Phi \tag{27}$$

$$\kappa v=-\frac{\partial p}{\partial\xi} \tag{28}$$

$$\rho\theta=1+\Pi p \tag{29}$$

Having completed the formulation, we proceed next with the analysis of the structure of the reaction zone and then with that of the combustion zone. The analysis is very similar to that presented in [3] and for this reason many details will not be presented.

5 REACTION ZONE

To analyze the structure of this zone, under the condition $Z\gg 1$, we stretch the longitudinal moving coordinate, $X=Z\xi$, and expand the dependent variables in an asymptotic series in terms of Z^{-1}. Following [3] it can be shown that, to leading order, temperature, concentration, pressure and density are independent of X, thus

$$\begin{aligned}
\theta &\sim \theta^o(t)+Z^{-1}\theta^1(X,t)+\ldots,\\
Y &\sim Y^o(t)+Z^{-1}Y^1(X,t)+\ldots,\\
p &\sim p^o(t)+Z^{-1}p^1(X,t)+\ldots,\\
\rho &\sim \rho^o(t)+Z^{-1}\rho^1(X,t)+\ldots,\\
\eta &\sim \eta^o(X,t)+\ldots,\\
v &\sim v^o(X,t)+\ldots,\\
f &\sim f^o(t)+\ldots.
\end{aligned} \tag{30}$$

After substitution in the governing equations, we found the following: To leading-order, the pressure is constant within the reaction zone. Combining the energy equation with the fuel balance shows that the leading-order terms are $O(Z^{-1})$, in which case only conduction in the X direction and reaction participate

$$\frac{\partial^2 \theta^1}{\partial X^2} = q f_t^o \frac{\partial \eta^o}{\partial X} \tag{31}$$

(Note that to leading order, the heat loss term is $Z^{-1}\dot{Q}_{hD}$). Integration, using the boundary conditions $\partial\theta^1/\partial X = 0$, $\eta^o = 1$ as $X \to -\infty$, yields

$$\frac{\partial \theta^1}{\partial X} = -q f_t^o (1 - \eta^o) \tag{32}$$

For the oxygen mass balance, a similar analysis shows that the leading-order terms are convection, diffusion and reaction,

$$Le \rho^o Y^o(t) \frac{\partial v^o}{\partial X} - \rho^o \frac{\partial^2 Y^1}{\partial X^2} = \mu Le f_t^o \frac{\partial \eta^o}{\partial X}, \tag{33}$$

where we have taken into account that ρ^o is constant. A second integration gives

$$Le \rho^o Y^o(t) v^o - \rho^o \frac{\partial Y^1}{\partial X} = \mu Le f_t^o \eta^o + \text{const} \tag{34}$$

The total gas mass balance reads

$$\rho^o \frac{\partial v^o}{\partial X} = -\mu_g f_t^o \frac{\partial \eta^o}{\partial X}. \tag{35}$$

and after integration

$$\rho^o v^o = -\mu_g f_t^o \eta^o + \text{const}. \tag{36}$$

Finally, the equation for the fuel mass is expressed to leading-order as

$$f_t^o \frac{\partial \eta^o}{\partial X} = -a_s^o \left\{ \frac{\left(Y^o(t) + Z^{-1} Y^1(X,t)\right)\left(1 + \Pi p^o(t)\right)}{\theta^o(t) + Z^{-1}\theta^1(X,t)} \right\} \psi(\eta^o) e^{\theta^1} \tag{37}$$

From the above, we can now determine the jumps in heat, oxygen mass and gas mass fluxes across the front in terms of the jump in the depth of fuel conversion. Thus,

$$\left. \frac{\partial \theta^1}{\partial X} \right|_{-\infty}^{\infty} = -q f_t^o \tag{38}$$

$$\rho^o \left. \frac{\partial Y^1}{\partial X} \right|_{-\infty}^{\infty} = \left(\mu + Y^o(t)\mu_g\right) Le f_t^o \tag{39}$$

$$\rho^o v^o \Big|_{-\infty}^{\infty} = \mu_g f_t^o \tag{40}$$

Multiplying equation (32) by (37) yields

$$q \left(f_t^o\right)^2 \left(\frac{1-\eta^o}{\psi(\eta^o)} \right) \frac{\partial \eta^o}{\partial X} = -a_s^o \left\{ \frac{Y^o(t)(1 + \Pi p^o(t))}{\theta^o(t)} \right\} e^{\theta^1} \frac{\partial \theta^1}{\partial X} \tag{41}$$

which can be further integrated across the reaction zone to give

$$f_t^o = \sqrt{\frac{a_s^o \left\{Y^o(t)(1 + \Pi p^o(t))\right\}}{q\theta^o(t) I_\eta}}, \qquad I_\eta = \int_0^1 \frac{(1-\eta^o)}{\psi(\eta^o)} d\eta^o. \tag{42}$$

This expression specifies the velocity of the front in terms of the mole fraction Y^o and the temperature θ^o of the reaction zone. In the above, we have assumed full consumption of the fuel at the front.

6 THE COMBUSTION ZONE

Consider, next, the combustion zone structure, where, chemical reaction rates are insignificant. To analyze this problem, we must consider the conservation equations on either side of the reaction front, across which the jump conditions derived previously apply. These relations are used next to provide the profiles inside the combustion zone. Consider, first, oxygen, total gas and fuel mass balances, and denote leading order terms with subscript o. Under steady-state conditions, we have the following

$$\rho_o B_o \frac{\partial Y_o}{\partial \xi} - \frac{1}{Le}\frac{\partial}{\partial \xi}\left(\rho_o \frac{\partial Y_o}{\partial \xi}\right) = 0 \tag{43}$$

$$\frac{\partial}{\partial \xi}(\rho_o B_o) = 0 \qquad \text{where} \qquad B_o = v_o - \phi f_t^o \tag{44}$$

$$\frac{\partial \eta_o}{\partial \xi} = 0 \tag{45}$$

Darcy's law and the ideal gas law read

$$\frac{\partial p_o}{\partial \xi} = 0 \qquad \text{and} \qquad \rho_o \theta_o = \text{const.} \tag{46}$$

Because $B_o > 0$, the solution for Y in $\xi > 0$ must be a constant independent of ξ. Equation (44) also shows that $\rho_o B_o$ is a constant. Then, by integrating (43) in $\xi < 0$, where ρ_o is constant, and making use of the jump condition across the reaction front, we obtain

$$Y_o = \begin{cases} 1 - \left(\dfrac{(\mu + Y_b \mu_g) f_t^o}{\rho_o B_o^-}\right) \exp\left(Le B_o^- \xi\right) & : \quad \xi < 0 \\ Y_b(t) & : \quad 0 < \xi \end{cases}$$

This equation provides the profile of the mass fraction upstream of the reaction front. Y_b is obtained using the jump condition across the reaction zone, $[Y_o] = 0$:

$$Y_b = \frac{v^- - (\rho_o^- \phi + \mu) f_t^o}{v^- + (\mu_g - \rho_o^- \phi) f_t^o} \cong \frac{v^- - \mu f_t^o}{v^- + \mu_g f_t^o}. \tag{47}$$

Note that for $Y_b > 0$, the condition $v^- > \mu f_t$ must apply, namely the total gas mass flux should be sufficiently large. Next, equation (45) gives

$$\eta_o = \begin{cases} 1 & : \quad \xi < 0 \\ 0 & : \quad 0 < \xi \end{cases}$$

assuming, again, complete fuel combustion. Finally, taking $\Pi \ll 1$, and inserting equation (47) into equation (42) gives

$$V_D^2 \approx \mathcal{A}\,\theta_f \exp\left(-\frac{\gamma}{\theta_f}\right)\left(\frac{1-\mu V_D}{1+\mu_g V_D}\right) \tag{48}$$

where we have defined the dimensionless variables

$$\mathcal{A} = \frac{\tilde{a}_s \alpha_s k_o \tilde{Y}_o \tilde{p}_i}{q\gamma R \tilde{T}_o I_\eta v_i^2} \quad \text{and} \quad \gamma = \frac{E}{R\tilde{T}_o}. \tag{49}$$

Equation (48) is one relation relating the unknown leading-order velocity of the front, $V_D \equiv f_t^o$, to the front temperature, θ_f. A second relation is obtained by solving the heat balance in the combustion zone. For this, we must consider three cases, adiabatic combustion, heat loss by convection and heat loss by conduction.

6.1 The Adiabatic Case

In the adiabatic case, the heat loss term does not contribute and the energy balance reads

$$A_o \frac{\partial \theta_o}{\partial \xi} - \frac{\partial^2 \theta_o}{\partial \xi^2} = 0 \tag{50}$$

where

$$A_o = a\rho_o v_o - f_t^o \approx -f_t^o < 0 \tag{51}$$

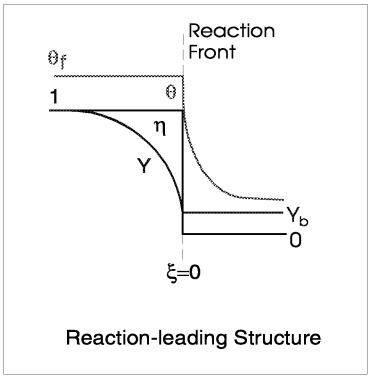

Figure 4: The Adiabatic Case: Schematic profiles of temperature, oxygen mass fraction and fuel conversion in the combustion zone.

Because $A_o < 0$, the only possible solution for $\xi < 0$ is a constant, independent of ξ. For $\xi > 0$, we integrate (50) and make use of the jump condition at the reaction front to obtain

$$\theta_o = \begin{cases} \theta_f(t) & : \quad \xi < 0 \\ 1 - \left(\dfrac{q f_t^o}{A_o^+}\right) \exp\left(A_o^+ \xi\right) & : \quad 0 < \xi \end{cases}$$

showing that the temperature decays exponentially fast downstream of the combustion front. A similar result was obtained in [3]. In conjunction with the continuity of temperature at $\xi = 0$, $[\theta_o]_-^+ = 0$, the above gives an expression for the dimensionless front temperature,

$$\theta_f = 1 - \frac{q V_D}{A_o^+} \tag{52}$$

where $A_o^+ \equiv a\mu_g V_D - V_D$. Equation (52) shows that the front temperature depends not only on the available heat content of the fuel, i.e., paramater q, but also on the gas mass influx and the net gas production at the front. If $a\mu_g V_D \ll 1$, then θ_f is the adiabatic temperature rise,

$$\theta_f = 1 + q. \tag{53}$$

Figure 4 shows schematic profiles of temperature, mass fraction and conversion across the combustion zone for the adiabatic case.

6.2 The Non-adiabatic Case

Consider, next, the temperature profile for the non-adiabatic case. We will consider separately the two different mode, convective and conductive heat losses.

6.2.1 Convective heat losses

For the convective mode case, the energy equation reads

$$A_o \frac{\partial \theta_o}{\partial \xi} - \frac{\partial^2 \theta_o}{\partial \xi^2} = -h(\theta_o - 1) \tag{54}$$

where h is the dimensionless heat transfer coefficient

$$h = \frac{\tilde{h} t^*}{(1-\phi) c_s \rho_s H} \tag{55}$$

The solution of (54) is readily found

$$\theta_o = \begin{cases} 1 + (\theta_f(t) - 1)\exp\left\{\frac{1}{2}\left(c_1^- + \sqrt{(c_1^-)^2 + 4h}\right)\xi\right\} & : \quad \xi < 0 \\ 1 + (\theta_f(t) - 1)\exp\left\{\frac{1}{2}\left(c_1^+ - \sqrt{(c_1^+)^2 + 4h}\right)\xi\right\} & : \quad 0 < \xi \end{cases}$$

where $c_1^{\pm} = A_o^{\pm}$. Note that $\theta_o \to 1$ as $\xi \to \pm\infty$. This result describes the temperature profile inside the combustion zone. Using the jump condition for the heat flux across the reaction front gives

$$\theta_f = 1 - \frac{2qV_D}{A_o^+ - \sqrt{(A_o^+)^2 + 4h} - A_o^- - \sqrt{(A_o^-)^2 + 4h}}, \tag{56}$$

which when $a\mu_g V_D \ll 1$, further simplifies to

$$\theta_f = 1 - \frac{q}{\frac{a\mu_g}{2} - \sqrt{1 + \frac{4h}{V_D^2}}} \tag{57}$$

Corresponding temperature profiles for this case are shown in Figure 5, for different volumetric heat transfer coefficients.

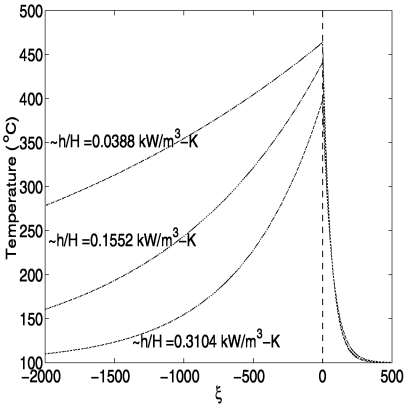

Figure 5: Temperature profiles for nonadiabatic combustion fronts with the convective type heat losses. The injection velocity is 100 m/day.

6.2.2 Conductive Heat Losses

When heat losses occur by conduction in a direction perpendicular to the flow direction (Fig. 1b), the heat transfer coefficient is *time-dependent* and the previous analysis does not apply. An expression for the heat losses in this case was developed by Yortsos and Gavalas [20], in terms of the local temperature history. In the dimensional moving coordinate system $\tilde{\xi} = \tilde{x} - V\tilde{t}$ the steady-state dimensional energy balance reads [20]

$$(c_g\rho_g\tilde{v} - (1-\phi)c_s\rho_s V)\,\frac{\partial\tilde{T}}{\partial\tilde{\xi}} = \lambda\frac{\partial^2\tilde{T}}{\partial\tilde{\xi}^2} + \frac{2\sqrt{(\lambda_h c_h\rho_h V)}}{H\sqrt{\pi}}\int_0^\infty \frac{\partial\tilde{T}}{\partial\tilde{\xi}}(\tilde{\sigma}+\tilde{\xi})\frac{d\tilde{\sigma}}{\sqrt{\tilde{\sigma}}}, \tag{58}$$

We may use the previous notation to express the above equation in terms of the dimensionless moving coordinate ξ. For convenience, however, we will introduce a slightly different notation and use the variable

$$\xi' = \frac{\xi}{x_*} \tag{59}$$

where

$$x_* = \frac{\tau}{V_D^{1/3}} \quad \text{and} \quad \tau \equiv \left(\frac{Hv_i}{2\alpha_s}\right)^{2/3} \tag{60}$$

In this notation, the dimensionless balance is

$$\frac{1}{\bar{\mu}}\frac{\partial\theta}{\partial\xi'} = \frac{\partial^2\theta}{\partial\xi'^2} + \frac{1}{\sqrt{\pi}}\int_0^\infty \frac{\partial\theta}{\partial\xi'}(\sigma+\xi')\frac{d\sigma}{\sqrt{\sigma}} \tag{61}$$

where

$$\bar{\mu} \approx \frac{V_D^{1/3}}{A_o\tau} \tag{62}$$

and where we assumed for simplicity $\alpha_s \approx \alpha_h$. Because $A_o^- = -V_D$ and $A_o^+ = a\mu_g V_D - V_D$, $\bar{\mu}$ is different ahead and behind the front. Defining $\varphi = \partial\theta/\partial\xi'$, equation (61) further simplifies to

$$\frac{1}{\bar{\mu}}\varphi(\xi') = \varphi'(\xi') + \frac{1}{\sqrt{\pi}}\int_0^\infty \varphi(\sigma+\xi')\frac{d\sigma}{\sqrt{\sigma}}. \tag{63}$$

For its solution of we need to consider the two different regions, ahead and behind the front.

i - *Ahead of the Front,* $\xi' > 0$

In this region, Equation (63) becomes

$$\frac{1}{\bar{\mu}_+}\varphi_+(\xi') = \varphi'_+(\xi') + \frac{1}{\sqrt{\pi}}\int_0^\infty \varphi_+(\sigma+\xi')\frac{d\sigma}{\sqrt{\sigma}} \tag{64}$$

which must be solved subject to the boundary conditions

$$\begin{aligned} \xi' &= 0, \qquad \theta = \theta_f \\ \xi' &\to \infty, \qquad \theta \to 1 \end{aligned} \tag{65}$$

The solution is an exponential

$$\varphi = c_3\,\exp(-z_1\xi'), \qquad \xi' > 0 \tag{66}$$

where $z_1 > -1/\bar{\mu}_+$ is the real positive root of the equation

$$\frac{\bar{\mu}_+^2}{z_1} - (1 + \bar{\mu}_+ z_1)^2 = 0. \tag{67}$$

Integrating we find an exponential decay

$$\theta = 1 + (\theta_f - 1)\exp(-z_1 \xi') \tag{68}$$

where the front temperature, θ_f, is to be determined.

ii - *Behind the Front,* $\xi' < 0$

Behind the front the energy balance reads

$$\frac{1}{\bar{\mu}_-}\varphi_-(\xi') = \varphi'_-(\xi') + \frac{1}{\sqrt{\pi}} \int_0^\infty \varphi(\sigma + \xi') \frac{d\sigma}{\sqrt{\sigma}} \qquad , \qquad \xi' < 0 \tag{69}$$

This integro-differential equation also includes information *ahead* of the front. When the temperature profile is smooth and there is no discontinuity at the front, we can rearrange the integral to read as follows

$$\frac{1}{\bar{\mu}_-}\varphi_-(\xi') = \varphi'_-(\xi') + \frac{1}{\sqrt{\pi}} \left(\int_0^{-\xi'} \frac{\varphi_-(\sigma + \xi')d\sigma}{\sqrt{\sigma}} + \int_{-\xi'}^\infty \frac{\varphi_+(\sigma + \xi')d\sigma}{\sqrt{\sigma}} \right) \qquad , \qquad \xi' < 0 \tag{70}$$

The second term in parantheses can be expressed using (68). We obtain

$$\frac{1}{\bar{\mu}_-}\varphi_-(\xi') = \varphi'_-(\xi') + (1 - \theta_f)\sqrt{z_1}\, \exp(-z_1\xi')\, \mathrm{erfc}(\sqrt{(-z_1\xi')}) + \frac{1}{\sqrt{\pi}} \int_0^{-\xi'} \frac{\varphi_-(\sigma + \xi')d\sigma}{\sqrt{\sigma}}. \tag{71}$$

Defining $\zeta = -\xi'$, $\varphi_-(\xi') \equiv h(\zeta)$, this further reads

$$\frac{1}{\bar{\mu}_-}h(\zeta) = -h'(\zeta) + (1 - \theta_f)\sqrt{z_1}\, \exp(z_1\zeta)\, \mathrm{erfc}(\sqrt{(z_1\zeta)}) + \frac{1}{\sqrt{\pi}} \int_0^\zeta \frac{h(\varrho)d\varrho}{\sqrt{(\zeta - \varrho)}} \tag{72}$$

For simplicity, we will solve this equation by neglecting the conduction term along the flow direction (first term on the RHS). We take a Laplace transform

$$\mathcal{H}(s) = \left(\frac{(1-\theta_f)\bar{\mu}_- \sqrt{z_1}}{(\sqrt{s}+\sqrt{z_1})(\sqrt{s}-\mu_-)} \right) \tag{73}$$

the inversion of which gives

$$h(\zeta) = \frac{(1-\theta_f)\bar{\mu}_- \sqrt{z_1}}{\bar{\mu}_- + \sqrt{z_1}} \left(\sqrt{z_1} \exp(z_1\zeta)\,\mathrm{erfc}(\sqrt{(z_1\zeta)}) + \bar{\mu}_- \exp(\bar{\mu}_-^2\,\zeta)\ \mathrm{erfc}(-\bar{\mu}_-\sqrt{\zeta}) \right) \tag{74}$$

To find the temperature, we use the boundary conditions

$$\begin{aligned} \xi' &= 0, & \theta &= \theta_f \\ \xi' &\to -\infty, & \theta &\to 1. \end{aligned} \tag{75}$$

After one more integration, the temperature behind the front is found

$$\begin{aligned} \theta \approx \theta_f + \frac{(1-\theta_f)\bar{\mu}_- \sqrt{z_1}}{\bar{\mu}_- + \sqrt{z_1}} \\ \times \left(\frac{1}{\sqrt{z_1}} [1 - \exp(-z_1\xi')\,\mathrm{erfc}(\sqrt{(-z_1\xi')})] + \frac{1}{\bar{\mu}_-} [1 - \exp(-\bar{\mu}_-^2\,\xi')\,\mathrm{erfc}(-\bar{\mu}_-\sqrt{(-\xi')})] \right). \end{aligned} \tag{76}$$

Equations (68) and (76) can be used to evaluate the heat fluxes across the reaction front. After some calculations, we find that the front temperature satisfies the equation

$$\theta_f = 1 + \frac{q\tau V_D^{2/3}}{(z_1 - \bar{\mu}_-\sqrt{z_1})}. \tag{77}$$

Having obtained θ_f, the temperature profiles ahead and behind the reaction front can be calculated. Typical temperature profiles for the case of conductive losses are shown in Figure 6. The three profiles correspond to three different steady-state solutions, obtained as will be explained subsequently.

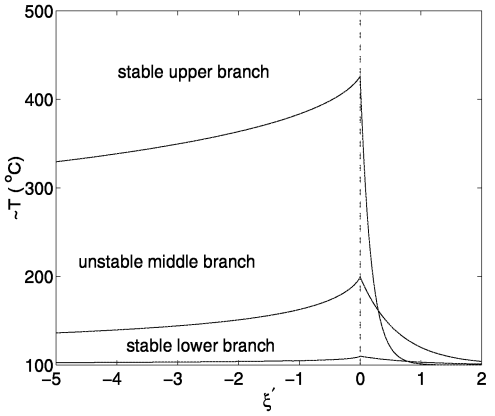

Figure 6: Temperature profiles for nonadiabatic combustion fronts with conductive type heat losses (H=0.5m).

Before we proceed further, we need to mention that in case the temperature ahead of the front is flat and a discontinuity arises at the front, namely if

$$\theta = \mathcal{H}(-\xi')[\theta(\xi') - 1] + 1 \tag{78}$$

the energy balance behind the front (69) takes the different expression

$$\frac{1}{\bar{\mu}_-}\varphi_-(\xi') = \varphi'_-(\xi') + \frac{1}{\sqrt{\pi}}\int_0^{-\xi'} \frac{\varphi_-(\sigma+\xi')d\sigma}{\sqrt{\sigma}} - \frac{1}{\sqrt{\pi}}\frac{(\theta_f - 1)}{\sqrt{(-\xi')}} \tag{79}$$

This equation can also be solved by methods similar to the previous.

In summary, by analyzing the heat transfer in the combustion zone, we have obtained a second relation, in addition to (48), to relate the front temperature to the front velocity. This relation is given by (52), (56) or (77), for the adiabatic case, the convective heat loss case or the case of conductive heat loss, respectively and involves a combination of parameters including q, γ, h, and τ. The solution of the set of the two equations are analyzed for the three different cases using a typical data set Table 1.

Table 1: Typical values of parameters for in-situ combustion

Parameter	Value
$\tilde{Q}$	39542 kJ/kg fuel
E	7.35*10^4 kJ/kmole
R	8.314 kJ/kmole-K
$\tilde{a}_s$	1.41*10^4 m^2/m^3
k_o	227 kW-m/atm-kmole
$\tilde{T}_o$	373.15 K
m, n, α	1
$\tilde{p}_i$	10 atm.
Y_i	1.0
$\tilde{h}/H$	0.0388 kW/m^3-K
D_M	2.014*10^{-6} m^2/s
λ	8.654*10^{-4} kW/m-K
ϕ	0.3
ρ_{gi}	1.2254 kg/m^3
c_g	1.0069 kJ/kg-K
ρ_f^o	19.2182 kg/m^3
c_s	1.0936 kJ/kg-K
$(1-\phi)\rho_s$	1.84*10^3 kg/m^3
M_f	235 kg/kmole
$\psi(\eta)$	1-η
H/C Ratio	1.65
$\tilde{\mu}$	3.018
$\tilde{\mu}_g$	1.000

Source: References [1],[4], [12] and [21]

7 RESULTS

7.1 The Adiabatic Case

In the adiabatic case, the two coupled equations have one unique solution. Thus, in the absence of heat losses, there is no multiplicity and a unique front velocity exists. The variables controlling the solution of this problem are q, a, μ_g, μ, γ and $\mathcal{A}$. The latter includes the combined effects of $\tilde{a}_s$, the kinetics, the pressure and the injection velocity. The effect of the injected oxygen mass fraction enters additionally through μ, while that of the initial fuel content enters also through μ_g. For $\mu_g > 0$, there is always one solution, $V_D < 1/\mu$. This is not necessarily the case for $\mu_g < 0$, where two solutions can exist, of which, however, only one is acceptable.

Figure 7 shows the variation of the front temperature as a function of the dimensionless parameter $\mathcal{A}$ for different values of γ. The temperature increases as $\mathcal{A}$ decreases, namely as the injection velocity increases and/or as the oxygen mass fraction, the pressure or the kinetic coefficient decrease. A specific illustration of the injection velocity influence is shown in Figure 8, for different values of γ. As expected the front temperature increases with increasing γ. Analogous effects on other important front variables, namely the front velocity and the oxygen mass fraction of the front are obtained likewise. Figure 9 shows a plot of the front velocity as a function of the injection velocity for different values of the injected mass fraction. The front velocity increases non-linearly with the injection velocity, the rate of increase decreasing at higher velocities. As expected, increasing the injected mole fraction leads to increase in the velocity. Figure 10 shows the non-dimensional unburned oxygen mass fraction at the front, as a function of the injection velocity. The effect is analogous to that of the front velocity.

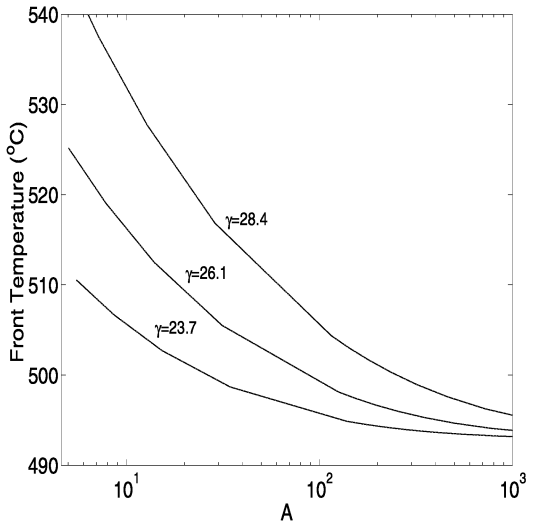

Figure 7: Adiabatic front temperature versus $\mathcal{A}$ for different values of γ.

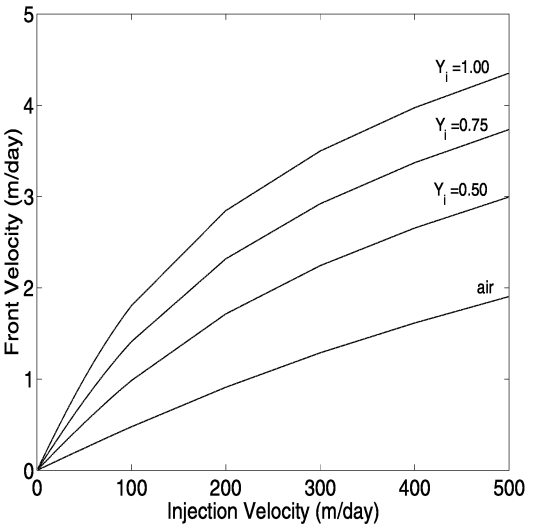

Figure 9: Adiabatic front velocity versus injection velocity for different values of injected oxygen mass fraction Y_i.

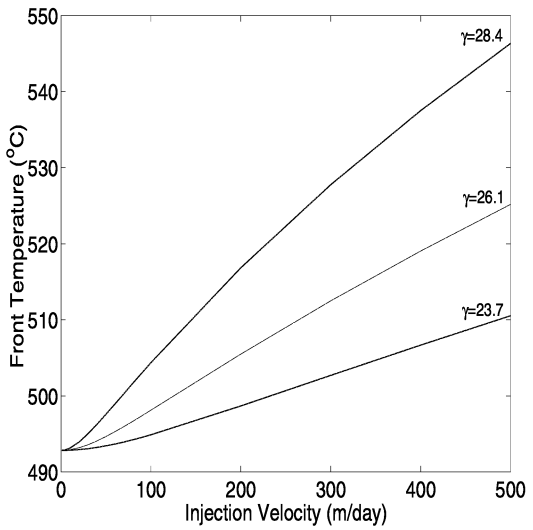

Figure 8: Adiabatic front temperature versus injection velocity for different values of γ.

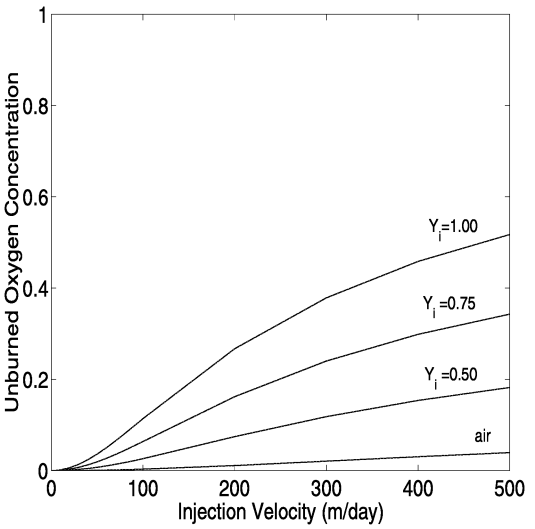

Figure 10: Unburned oxygen concentration for adiabatic front versus injection velocity for different values of injected oxygen mass fraction Y_i.

7.2 The Non-adiabatic Case: a. Convective Heat Losses

Subsequently we examined for the non-adiabatic case the sensitivity to variations in parameters, in particular the volumetric heat transfer coefficient $\tilde{h}/H$, for the typical values given in Table 1.

In contrast to the unique solution found for the adiabatic case, a multiplicity exists for the case of heat losses, provided that the injection velocity exceeds a critical threshold, E_c. As shown in Figures 11 and 12, the solution consists of a low temperature branch in the vicinity of the initial temperature, a high temperature branch and an intermediate branch connected to the latter. The lower branch practically corresponds to extinction (quenching). Above the threshold, three separate solutions exist for any given injection velocity. The existence and stability of these branches are investigated in the Appendix.

As shown in Figure 12, if the solution lies on the high-temperature branch, where rigorous combustion takes place, and subsequently the injection velocity decreases, then due to the increasingly dominating heat losses to the surrounding, the threshold E_c with an infinitely large slope is reached. Since the intermediate branch is unstable, a rapid transition to the lower branch occurs, corresponding to extinction. Hence, the threshold E_c is the exiction point. This type of behavior is unique to combustion and extensively reported in the literature, e.g., in premixed flames and well-stirred reactors.

The upper branch is the solution corresponding to a proper combustion front. It approaches and runs parallel to the adiabatic temperature solution. For a given heat transfer coefficient, the sensitivity of the front temperature to the injection velocity is very large near the threshold, but becomes almost negligible above it. Such behavior is typical of multiple solutions in other areas in reaction engineering. An increase in the heat transfer coefficient or a decrease in the reservoir thickness, both result in lowering the ultimate combustion temperature, and in increasing the ignition temperature and the velocity threshold. This is as expected, as higher rates of heat transfer and/or thinner formations lead to larger heat losses. We remark that the lowest value of heat transfer coefficient used in Figure 12 is about double the value used by Gottfried [9] in his investigation.

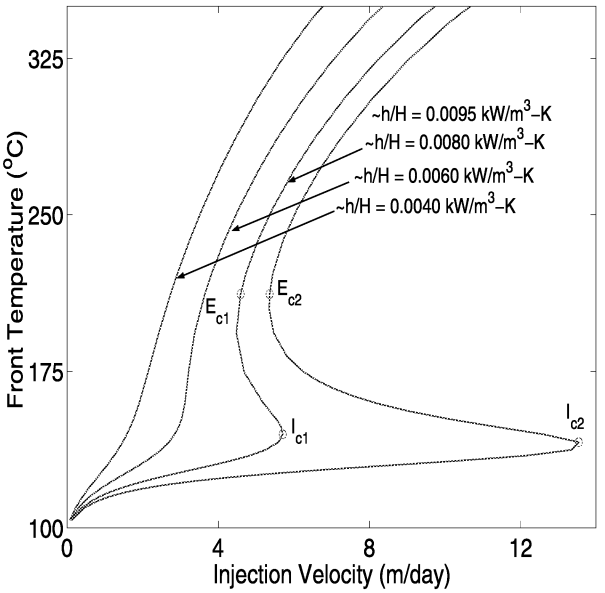

Figure 11: Non-adiabatic front temperature versus injection velocity for different values of the volumetric heat transfer coefficient, $\tilde{h}/H$. The extinction thresholds are I_{c1}=(5.7,144.8), E_{c1}=(4.6,211.4), I_{c2}=(13.5,141.0), E_{c2}=(5.4,211.9).

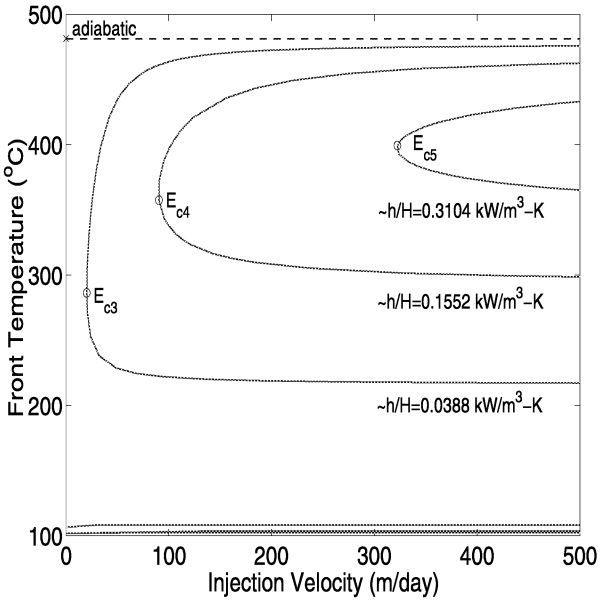

Figure 12: Non-adiabatic front temperature versus injection velocity for different values of the volumetric heat transfer coefficient, $\tilde{h}/H$. The extinction thresholds are E_{c3}=(20.2,286.2), E_{c4}=(90.4,357.5) and E_{c5}=(322.5,399.3).

Figure 13 shows the effect of the dimensionless parameter $\mathcal{A}$ on the front temperature for varying values of the heat transfer coefficient. The multiplicity is again apparent. Figure 14 illustrates the effect of the injected oxygen concentration on the front temperature. As the concentration decreases, the system approaches the extinction point E_c at a larger front temperature and injection velocity. This behavior is similar to the effect of varying the heat loss intensity. It is apparent in Figure 15 shows a plot of the front velocity as a function of the injection velocity. The muliplicity is apparent. It is also clear that the front velocity increases with the injection velocity. From a similar analysis, we can obtain the effect of the heat losses on the front velocity and the unburned oxygen concentration at the front (Figures 17 and 18). We note a multiplicity associated with both the front velocity and the unburned mass fraction. As expected, there exists a mass fraction branch that practically coincides with the injected mass fraction. The unburned oxygen mass fraction (Figure 16) increases with the injection rate and concentration.

Figure 19 illustrates the effect of q. This parameter includes the combined effects of parameters such as heat of reaction, initially available fuel, volumetric heat capacity of the solid and initial reservoir temperature. Although the stable temperature branch decreases and the unstable branch increases substantially as q decreases, the front temperature at the extinction point is not sensitive to changes in q. Similar was the effect of γ.

Subsequently, we investigated the critical extinction threshold (defined using the condition $(\partial V_D/\partial \mathcal{A}) \to \infty$). Along with equations (48) and (57) this allows us to compute the critical parameters V_{Dc}, θ_{fc} and $\mathcal{A}_c$. Figure 20 shows that the parameter space of injection velocity, oxygen mass fraction and volumetric heat transfer coefficient, is divided in two regions, one corresponding to sustained propagation and another to extinction. A surface delineates the two regions. Analogous plots can be obtained for other parameters.

We close this section by commenting on the effective Damköhler number. The characteristic time for reaction was given in [3]

$$t_R \equiv Z \left(\frac{k_o (Y_i \tilde{p}_i)^n e^{-E/R\tilde{T}_f}}{l_R^m (R\tilde{T}_o)^n} \right)^{-1}, \tag{80}$$

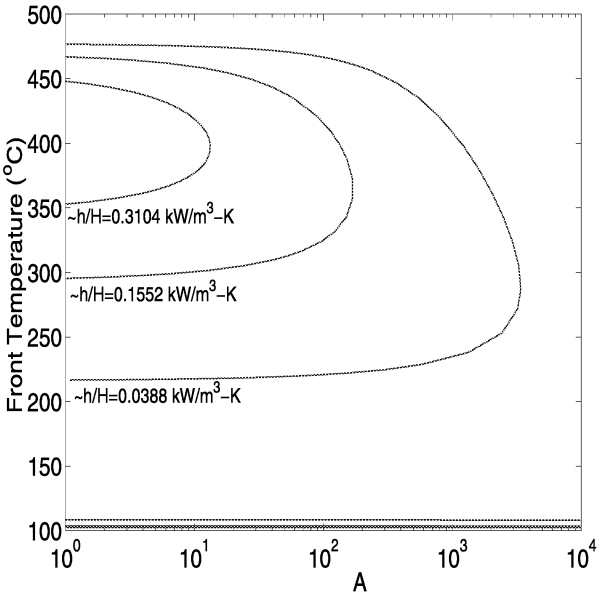

Figure 13: Non-adiabatic front temperature versus $\mathcal{A}$ for different values of the volumetric heat transfer coefficients.

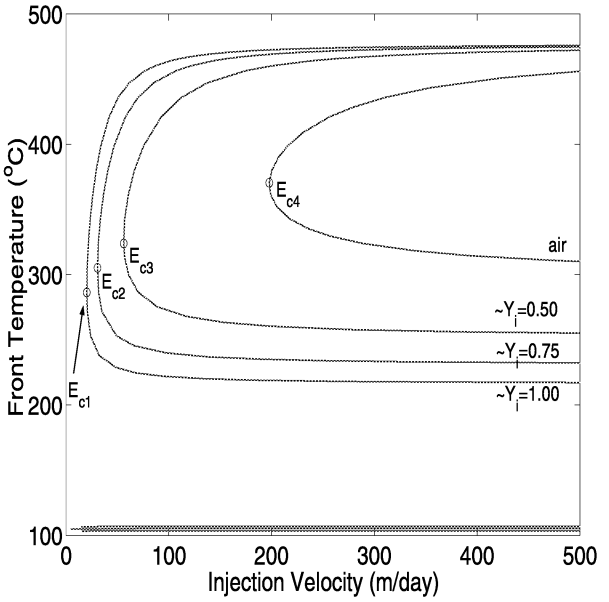

Figure 14: Non-adiabatic front temperature versus injection velocity for different values of the injected oxygen mass fraction Y_i. h/H=0.0388 kW/m^3-K, E_{c1}=(20.2,286.2), E_{c2}=(30.6,305.2), E_{c3}=(56.1,323.9), E_{c4}=(197.8,370.5).

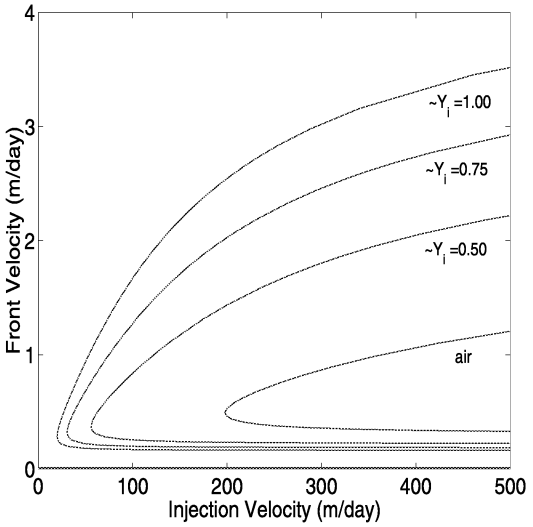

Figure 15: Non-adiabatic front velocity versus injection velocity for different values of the injected oxygen mass fraction Y_i.

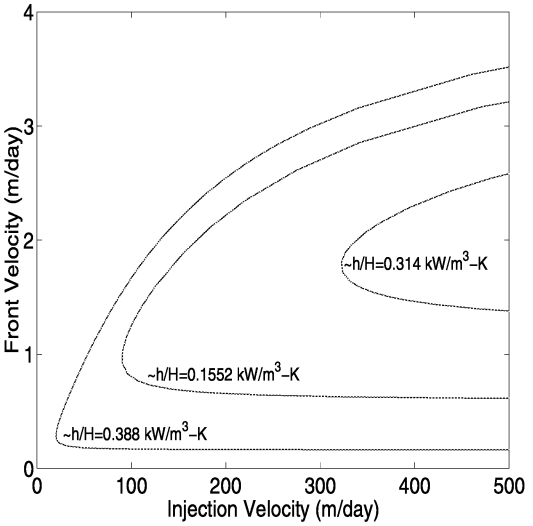

Figure 17: Non-adiabatic front velocity versus injection velocity for different values of the volumetric heat transfer coefficient. Front velocity for the lower stable branches are 0.01 m/day.

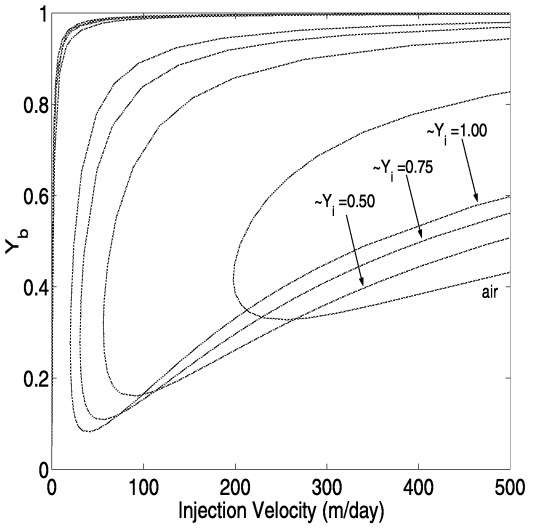

Figure 16: Non-dimensional unburned oxygen concentration for non-adiabatic front versus injection velocity for different values of the injected oxygen mass fraction Y_i.

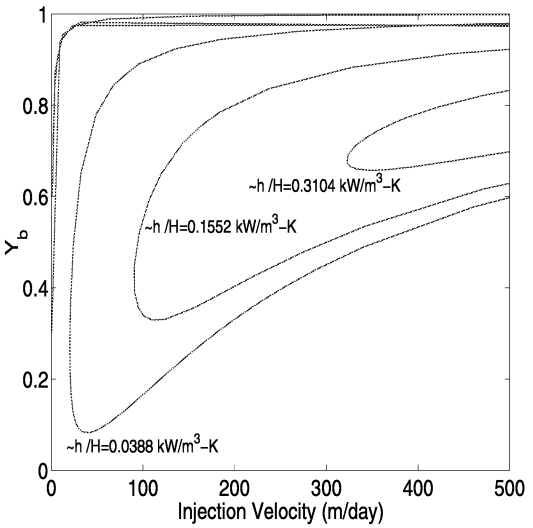

Figure 18: Non-dimensional unburned oxygen concentration for non-adiabatic front versus injection velocity with different values of the volumetric heat transfer coefficient.

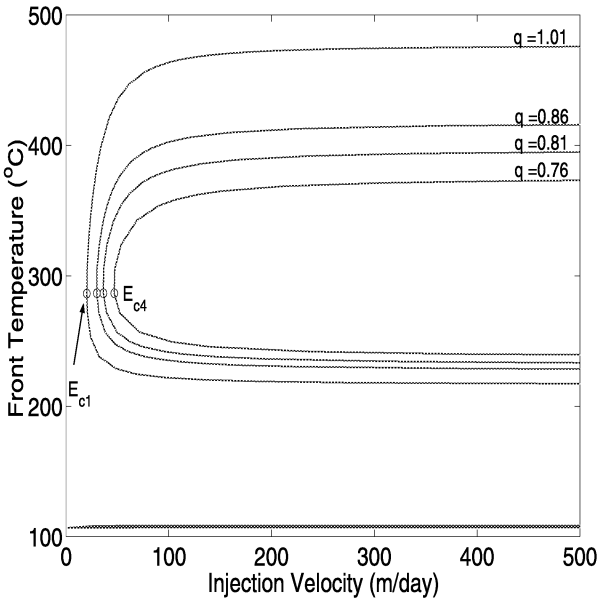

Figure 19: Non-adiabatic front temperature versus injection velocity for different values of q. $\tilde{h}/H$=0.0388 kW/m^3-K, E_{c1}=(20.2,286.2), E_{c2}=(30.0,286.6), E_{c3}=(36.3,286.6), E_{c4}=(46.9,286.6).

A characteristic time for the frontal advance (residence time) could be obtained using

$$t_F = \frac{l_T}{V_D \tilde{v}_o} \tag{81}$$

where l_T is the combustion zone thickness also given in [3]. The reaction rate and the rate of frontal advancement are inversely proportional to t_R and t_F respectively. The ratio of these characteristic times, called the Damköhler number, $Da = t_F/t_R$, could be used as an indication of how strongly the reaction kinetics control the combustion front. The calculated ratios for adiabatic and non-adiabatic cases are shown in Figure 21. When the system is adiabatic and the injection rate is $O(1)$ m/day, then $Da > 1$ and it is controlled by the injection velocity. This observation is in agreement with Kumar and Garon's experimental investigation of *in situ* combustion [22]. However, if the rate is larger or the system is non-adiabatic we observe that it is controlled by the kinetics of the reaction. A multiplicity corresponding to the three branches is also observed.

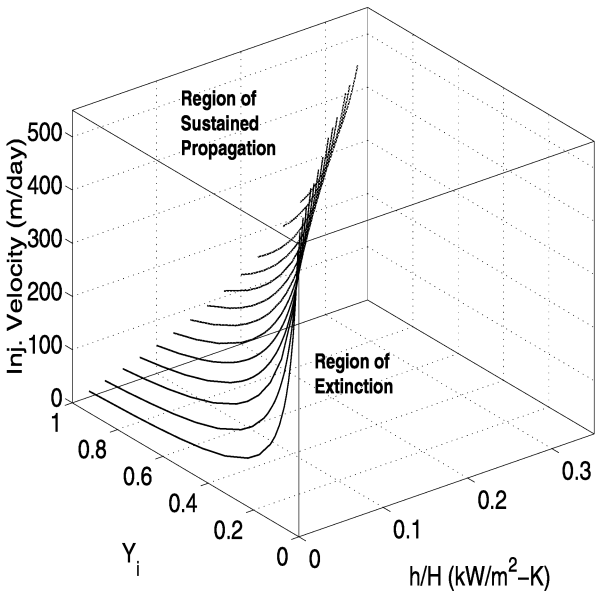

Figure 20: Injection velocity v_i versus injected oxygen mass fraction Y_i and the volumetric heat transfer coefficient $\tilde{h}/H$. The surface represents the calculated critical injection velocities.

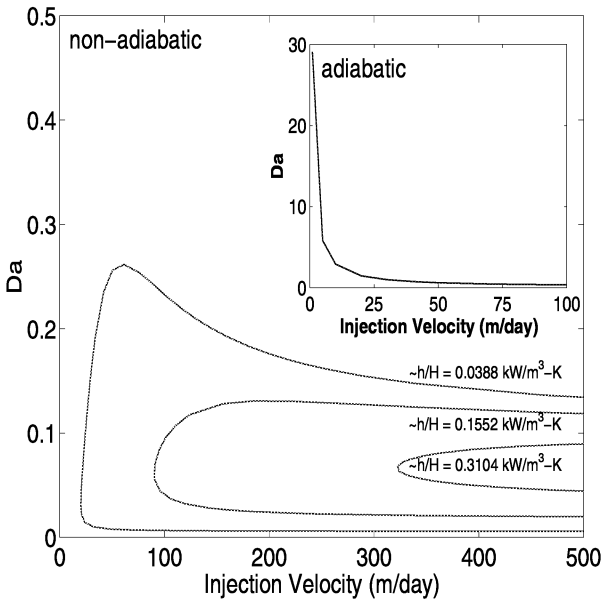

Figure 21: Damköhler number versus injection velocity.

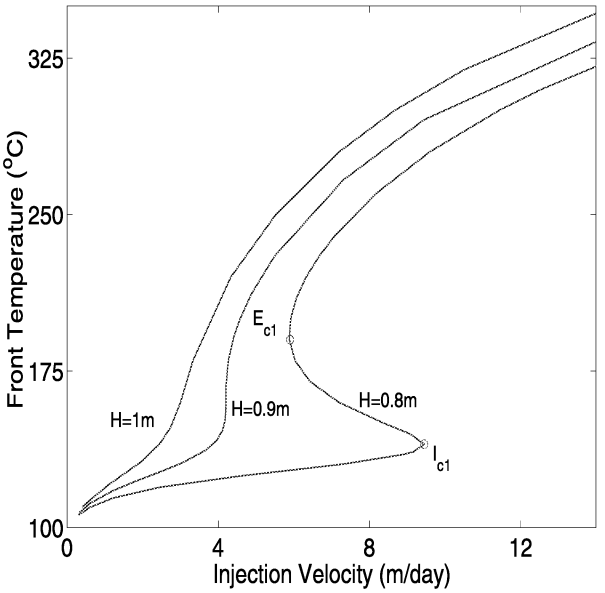

Figure 22: Non-adiabatic front temperature versus injection velocity obtained using the conductive heat loss model. I_{c1}=(9.45,140.0), E_{c1}=(5.9,190.0).

7.3 The Non-adiabatic Case: b. Conductive Heat Losses

Subsequently, we considered the effect of conductive heat losses. Equations (77) and (48) describe the steady-state solution in the presence of conductive heat losses. The two equations were solved simultaneously. Figures 22 and 23 show the front temperature behavior versus the injection velocity for varying thicknesses of the porous medium. A multiplicity analogous to the case of convective heat transfer is apparent. We studied the effect of heat losses by varying the reservoir thickness H, all other parameters being fixed. We note that the sensitivity of the extinction threshold to the reservoir thickness is significant for thickness values of the order of 1m or less. For larger values, the heat loss effect is not as significant. As H decreases, the extinction threshold rapidly increases, namely it requires an increasingly larger velocity for the reaction to be sustained. Figure 24 illustrates the effect of variable oxygen concentration on the front temperature.

Next, we attempted to compare the two non-adiabatic modes in more detail. For this purpose we tried to match the two mode results for a given reservoir thickness. Figure 25 shows that the upper branches can be made to overlap for a judicious choice of parameters (e.g. H=2m

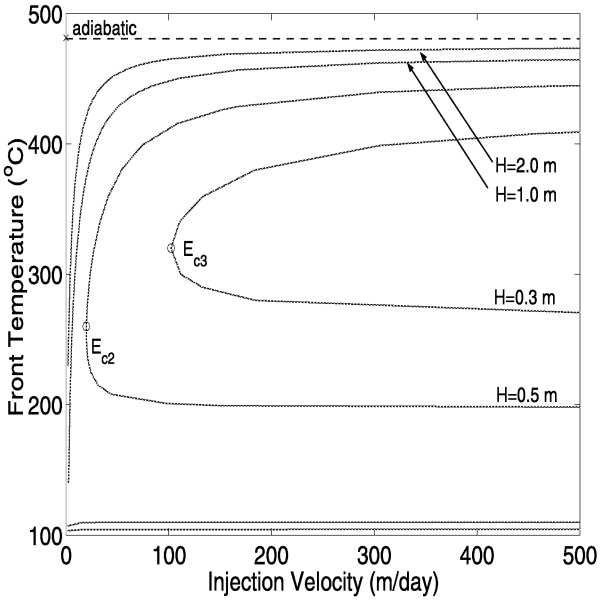

Figure 23: Non-adiabatic front temperature versus injection velocity obtained using the conductive heat loss model. E_{c2}=(19.7,260.0), E_{c3}=(102.1,320.0).

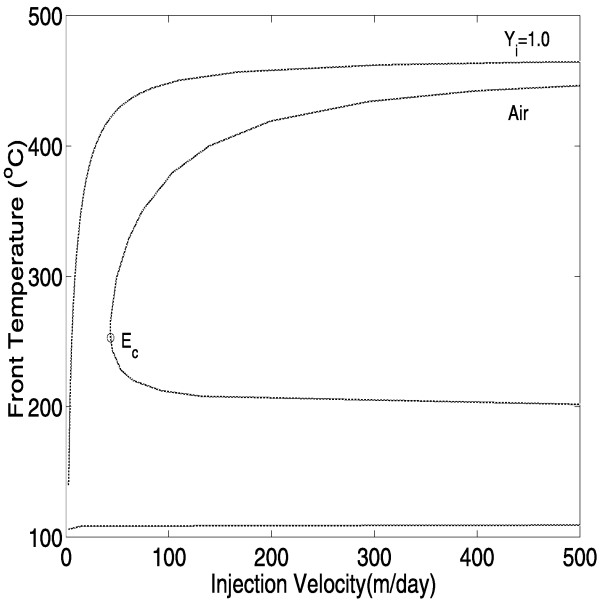

Figure 24: Non-adiabatic front temperature versus injection velocity for the cases of pure oxygen and air injection obtained using conductive type heat loss model. H=1m, E_c=(43.3,253).

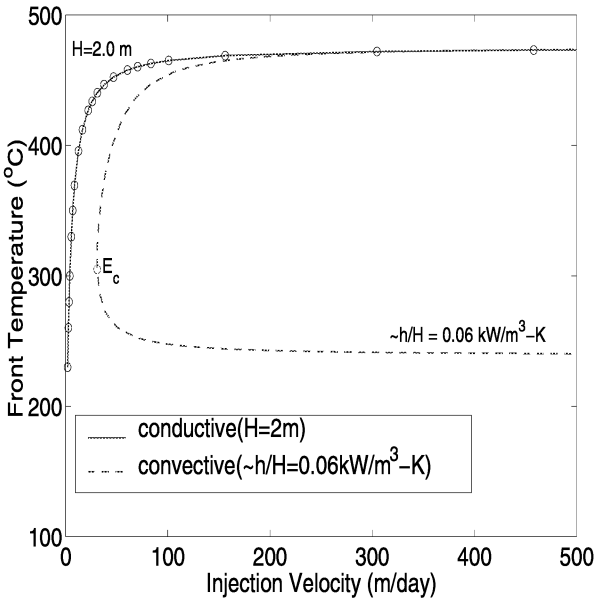

Figure 25: Non-adiabatic front temperature versus injection velocity. Comparison of the two non-adiabatic models. E_c=(30.9,305)

for the conductive and $\tilde{h}/H$=0.06 kW/m^3-K for the convective). Although the two models are in good agreement for high front temperatures and injection velocities, however, the results start to diverge with the decreasing velocities.

In the preceding sections, explicit expressions of the non-adiabatic front temperature were obtained, equations (57) and (77). From these we can attempt to express the overall heat transfer coefficient in terms of measurable parameters obtained using the conductive loss. By taking the dimensional form of these equations, defining $\omega = \frac{2\alpha_s}{HV}$ and re-arranging, we can express the film coefficient as

$$\tilde{h}(V, H, z_1) = \frac{1}{2}(1-\phi)c_s\rho_s V\left(\omega^{1/3}z_1^2 + 2\omega z_1^{3/2} + \omega^{5/3}z_1 - \omega^{-1}\right) \tag{82}$$

During the derivation of (82), the assumption $a\mu_g << 1$ is used. In equation (82), z_1 is the positive real root of equation (67) and is larger than $1/\omega$; V is the dimensional front velocity. We note that the coefficient is implicitely dependent on the front temperature because the non-adiabatic front velocity V is dependent on it. Figures 26 and 27 show the calculated values of the coefficient for varying reservoir thickness and injection velocity. The

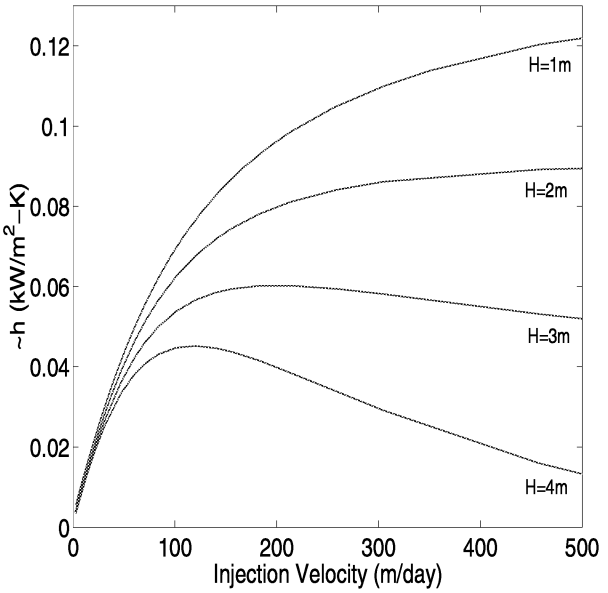

Figure 26: Overall heat transfer coefficient $\tilde{h}$ versus injection velocity v_i for varying reservoir thickness.

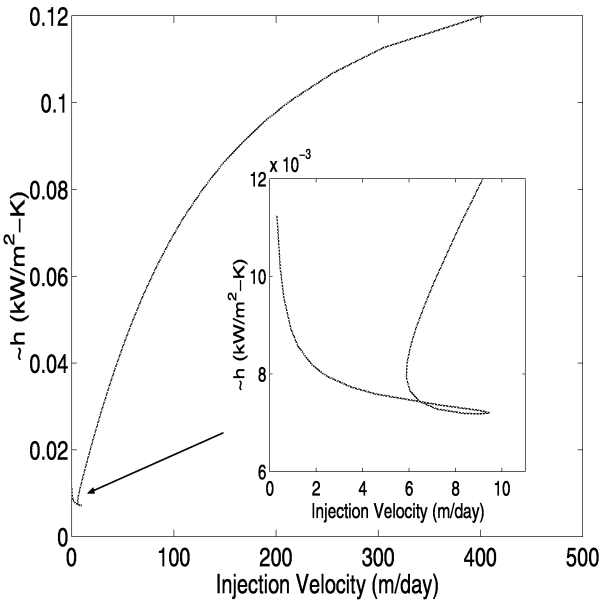

Figure 27: Overall heat transfer coefficient $\tilde{h}$ versus injection velocity v_i for H=0.8m.

coefficient first increases and subsequently decreases with the injection velocity, depending on the increasing reservoir thickness.

8 CONCLUDING REMARKS

In this report, we proposed a method for modeling the propagation of combustion fronts in porous media, by treating the reaction region as a place of discontinuity in the appropriate variables, which include, for example, fluxes of heat and mass. The reaction and combustion fronts have a spatially narrow width within which heat release rates, temperatures and species concentrations vary significantly. The narrow width calls for an approach in which these fronts are treated as surfaces of discontinuity.

Using a rigorous perturbation approach, similar to that used in the propagation of flames [6] and smoldering combustion [3], we derived appropriate jump conditions that relate the change in the variables across the front. The conditions account for the kinetics of the reaction between the oxygen and the fuel, the changes in the morphology of the pore space and the heat and mass transfer in the reaction zone. Then, the modeling of the problem reduces to the modeling of the dynamics of a combustion front, either side of which convective transport of momentum (fluids), heat and mass, but not chemical reactions, must be considered. Properties of the two regions are coupled using the derived jump conditions. This methodology allows to explicitly incorporate permeability heterogeneity effects in the process description, without the undue complexity of the coupled chemical reactions.

The analytical approaches developed herein reduces the rather complex combustion front propagation problem to a system of two coupled algebraic equations – for the front temperature and its propagation speed. Further, the latter equation (48) consists of a nondimensional quantity $\mathcal{A}$, reflecting the combined effects of inlet conditions as well as the above-mentioned physical and chemical properties. The effect of varying this parameter on the system dynamics was studied. Knowing the front temperature and propagation speed, explicit expressions, which allow to obtain the mass fraction of oxygen left unreacted as well as combustion and

reaction zone thicknesses, were derived. Non-adiabatic combustion fronts were also investigated by considering the heat losses to the surrounding with two different approaches (1) a convective type and (2) a conductive type. Analyses for a steadily propagating planar front were presented for typical values of *in situ* combustion. Extinction behavior due to heat losses was investigated in detail in the front temperature-injection velocity parameter space.

In the adiabatic case, the front temperature in the presence of gas mass influx is larger than the adiabatic temperature in terms of thermodynamic arguments only (i.e., $\theta_f = 1 + q$). However because typically $a\mu_g << 1$ the temperature difference due to mass influx is quite small. Therefore, a reasonable estimate for the adiabatic front temperature, in terms of dimensional quantities, is

$$\tilde{T}_f = \tilde{T}_o + \frac{Q\rho_f^o}{(1-\phi)c_s\rho_s}. \tag{83}$$

Note that the adiabatic front temperature in this form is independent of the front velocity. The dynamics of non-adiabatic combustion fronts appear to be markedly different. In this case, the developed models yield multiple steady states: one at low temperatures near the initial reservoir temperature, one at high temperatures above 300°C and one at intermediate temperatures. The intermediate branch is determined to be unstable. Among those, only the high temperature stable branch has the potential to lead to favorable conditions of oil displacement ahead of the front. Explicit expressions of non-adiabatic front temperature were obtained. Using $a\mu_g << 1$, the front temperature with the convective mode

$$\tilde{T}_{fconv} = \tilde{T}_o + \frac{Q\rho_f^o}{(1-\phi)c_s\rho_s\sqrt{1+\dfrac{4\lambda}{((1-\phi)c_s\rho_s V)^2}\left(\dfrac{\tilde{h}}{H}\right)}} \tag{84}$$

and with the conductive mode

$$\tilde{T}_{fcond} = \tilde{T}_o + \frac{Q\rho_f^o\left(\dfrac{HV}{2\alpha_s}\right)^{4/3}}{(1-\phi)c_s\rho_s\left[\left(\dfrac{HV}{2\alpha_s}\right)^{2/3} z_1 + \sqrt{z_1}\right]} \tag{85}$$

where again z_1 is the positive real root of equation (67). Obviously the non-adiabatic front temperature is always smaller than the adiabatic one and the difference becomes larger with increasing intensity of heat losses (i.e., larger $\tilde{h}$ or smaller H). Unlike the adiabatic front temperature, expressions (84) and (85) include the front velocity

$$V^2 = \left(\frac{\tilde{a}_s \lambda k_o \tilde{p}_i \tilde{T}_f}{Q \rho_f^o E}\right) \left(\frac{\rho_{gi} Y_i v_i - \tilde{\mu} \rho_f^o V}{\rho_{gi} v_i + \tilde{\mu}_g \rho_f^o V}\right) exp\left(-\frac{E}{R\tilde{T}_f}\right) \tag{86}$$

where the second term repesents the unburned oxygen concentration $\tilde{Y}_b$. Note that, whether the system is adiabatic or not, the front velocity is always influenced by the front temperature. We also observed that the effect of net gas production due to reaction (the term with $\tilde{\mu}_g$ in (86) on the front velocity is minimal and neglecting it overestimates the velocity with an $O(1)$ per cent error. Nevertheless an explicit expression for the front velocity could be obtained in the form of a quadratic polynomial equation.

We were also able to obtain an explicit expression for the overall heat transfer coefficient, (82). The coefficient is not only affected by the reservoir thickness, but also by the front dynamics. Figure 25 clearly demonstrated that, although we have chosen a reasonable average value for the film coefficient, the critical extinction threshold based on convective mode calculations only could be misleading. Previously, the transient behavior of the coefficient was analyzed for thermal fronts in porous medium in the absence of heat generating reactions such as hot water or steam injection. Experiments and analytical works show that its value decreases with respect to time and in the large-time limit, when steady-state condition becomes valid, levels off to a constant value [23].

In summary, we also found the following (1) The inlet conditions, i.e., injection rate and oxygen concentration, are crucial to the fate of a self-sustaining front. Higher injection rate of gas with higher fraction of oxygen prevents the extinction due to heat losses. (2) When the injection rate is fixed, the front speed increases (decreases) with the increasing (decreasing) front temperature, while the unburned oxygen concentration and the zone thicknesses decrease (increase). This behavior is similar to the premixed flames and points out the fact that the non-adiabatic front dynamics are limited by the reaction kinetics. The final

observation is further supported by the calculated Damköhler numbers (Fig. 21). (3) A nonadiabatic combustion front is thicker, cooler, travels slower and consumes less oxygen. (4) The zone thicknesses increase as the system approaches the extinction limit. (5) Away from the extinction region, the combustion zone thickness is always order of 0.1 meters (order of an inch) and about 6 times as large as that of the reaction zone. The very small thicknesses of these zones should be carefully considered in the implementation of direct numerical simulation of *in situ* combustion, particularly at the field scale. (6) A typical reservoir with a thickness equal to or larger than 2 m. behaves as an adiabatic system. (7) The most influential parameters on the front behavior are thickness of the reservoir, volumetric heat capacity of the solid matrix, heat of reaction, initially available fuel content and activation energy of the combustion reaction. We also noted that the initial temperature, i.e., the temperature corresponding to the vaporization zone, is as influential as the activation energy.

An interesting behavior of the system is observed when the heat content of the fuel is changed. This could be achieved by varying either the heat of the reaction, Q, or the initially available fuel amount, ρ_f^o. Note that these two parameters are included along with each other in both the front temperature and the front speed equations. Therefore, one would expect that same amount of change applied to one of the two would result in the same system response with the other. First, we increased parameter Q by a factor of 1.25, and observed that the front temperature increases so much that the front velocity increases as well although the latter is proportonal to $1/Q$. When the same calculation is repeated for ρ_f^o, an increased front temperature is similarly observed, however the front speed decreases. This observation illustrates clearly the effect of $\tilde{Y}_b$. The effect of fuel amount on the front propagation speed has been discussed in *in situ* combustion literature several times based on adiabatic combustion tube experiments (see for example [24]). Our observation is in agreement with these experiments and brings an insight to this particular behavior of the front.

The planar front analysis has not only given us insight to the nonadiabatic nature of the combustion fronts in porous media but also has revealed and, to a certain extent, quantified the importance of the natural environment where *in situ* combustion process may have limited applications. We have found that although, due to typical reservoirs, the majority of *in situ*

combustion processes may take place under nearly adiabatic conditions, extinction plays an important role on the dynamics of the combustion front.

The models developed do not include effects of the preceding zones, which are quite complex. The vaporization of interstitial hydrocarbons and water downstream, and the thermal cracking of the oil ahead of the unburned region should contribute to the dynamics of combustion front in terms of additional heat losses. On the other hand, LTO reactions between the oxygen left unreacted in the combustion front and the liquid oil phase could be a source of additional heat. Inclusion of these effects to an analytical work, such as presented here, is under consideration.

References

[1] Prats, M. *Thermal Recovery.* SPE Monograph Series SPE of AIME 1982.

[2] Aldushin, A.P. and Matkowsky, B.J., *Combust. Sci. Tech.* 133:293 (1998).

[3] Schult, D.A., Matkowsky, B.J., Volpert, V.A., and Fernandez-Pello, A.C., *Combust. Flame* 104:1 (1996).

[4] Boberg, T.C. *Thermal Methods of Oil Recovery.* An Exxon Monograph Series 1988.

[5] Durlofsky, L.J., Jones R.C. and Milliken, W.J., *Advances in Water Resources* 20:335 (1997).

[6] Matalon, M. and Matkowsky, B.J., *J. Fluid Mech.* 124:239 (1982).

[7] Pelcé, P., *Dynamics of Curved Fronts.* Academic Press 1988.

[8] Baily, H.R. and Larkin B.K., *Petroleum Trans.* AIME 219:320 (1960).

[9] Gottfried, B.S., *Soc. Pet. Eng. J.* 196-210 (1965).

[10] Beckers, H.L. and Harmsen, G.J., *Soc. Pet. Eng. J.* 231-49 (1970).

[11] Burger, J.G. and Sahuquet, B.C., *Soc. Pet. Eng. J.* 54-66 (1972).

[12] Ağca, C. and Yortsos, Y.C. *Steady-State Analysis of In Situ Combustion.* Presented at the Annual California Regional Meeting of the Society of Petroleum Engineers of AIME. Paper SPE 13624 447-362 (1985)

[13] Armento, M.E. and Miller, C.A. *Soc. Pet. Eng. J.* 423-430 (1977).

[14] Schult, D.A., Bayliss, A. and Matkowsky, B.J., *SIAM J. Appl. Math.* 58:806 (1998).

[15] Britten, J.A. and Krantz, W.B., *Combust. Flame* 60:125 (1985).

[16] Britten, J.A. and Krantz, W.B., *Combust. Flame* 65:151 (1986).

[17] Lu, C. and Yortsos, Y.C. *A Pore-Network Model of In Situ Combustion in Porous Media.* Presented at the Society of Petroleum Engineers (International) Thermal Operations and Heavy Oil Symposium. Paper SPE 69705 (2001).

[18] Benham A.L. and Poettmann, F.H., *Petroleum Trans.* AIME 213:28 (1958).

[19] Da-Mota J.C., Dantas, W.B., Gomes, M.E. and Marchesin, D., *Mat. Contemp.* 8:129 (1995).

[20] Yortsos, Y.C. and Gavalas, G.R., *Int. J. Heat Mass Transfer* 305:305 (1982).

[21] Vossoughi, S., Bartlett, G.W., Willhite, G.P., *Soc. Pet. Eng. J.* 656-663 (1985).

[22] Kumar, M. and Garon, A.M., *SPE Reservoir Eng.* 55-61 (1991).

[23] Zolotukhin, A.B. *Analytical Definition of the Overall Heat Transfer Coefficient.* Presented at the Annual California Regional Meeting of the Society of Petroleum Engineers of AIME. Paper SPE 7964 (1979).

[24] Martin, W.L., Alexander, J.D. and Dew, J.N., *Petroleum Trans.* AIME 213:28 (1958).

APPENDIX: Stability Analysis

We can interpret the observed multiplicity by conducting a stability analysis. The dimensionless rate of heat generation due to the combustion reaction is

$$\Phi_{rD} = qV_D \tag{87}$$

and the heat loss per unit bulk volume per unit time is

$$\Phi_{hD} = \int_{-\infty}^{+\infty} \dot{Q}_{hD} d\xi = \int_{-\infty}^{+\infty} h(\theta - 1) d\xi, \tag{88}$$

After integration and several manipulation the rate of heat release reads as

$$\Phi_{hD} = \frac{1}{2}(\theta_f - 1)\left(A_{ho}^{-} + \sqrt{(A_o^{-})^2 + 4h} - A_{ho}^{+} + \sqrt{(A_o^{+})^2 + 4h}\right). \tag{89}$$

The two variables Φ_{rD} and Φ_{hD} are plotted in Figures (28) and (29). The points of intersection represent equilibrium states where the rate of heat generation is equal to the rate of heat losses. Depending on the value of the injection velocity, one (Figure 28) or three (Figure 29) equilibrium points exist. Not all equilibrium points correspond to a stable solution. Consider, for example, the middle equilibrium state in Figure 29. A slight disturbance of equilibrium to the right, i.e., increasing the front temperature by a small amount, results into a lower rate of heat lost than the rate of heat generated, thus driving the sytem towards a continuously increasing temperature away from the equilibrium state. Similarly, a slight perturbation in the other direction, towards lower front temperatures, results into a higher rate of heat lost than the rate of heat generation and a subsequent continuous decrease of the temperature away from the equilibrium point. Therefore this state is unstable. Following a same reasoning, the other two equilibrium states are stable, as indicated.

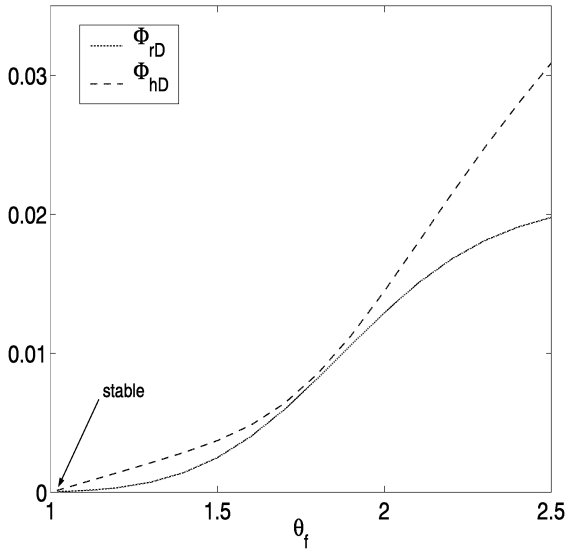

Figure 28: Nondimensional heat generation and loss rates versus nondimensional front temperature for convective type heat losses ($\tilde{h}/H$=0.3104 kW/m^3-K, injection velocity is 200 m/day). Only one steady-state exists corresponding practically to extinction.

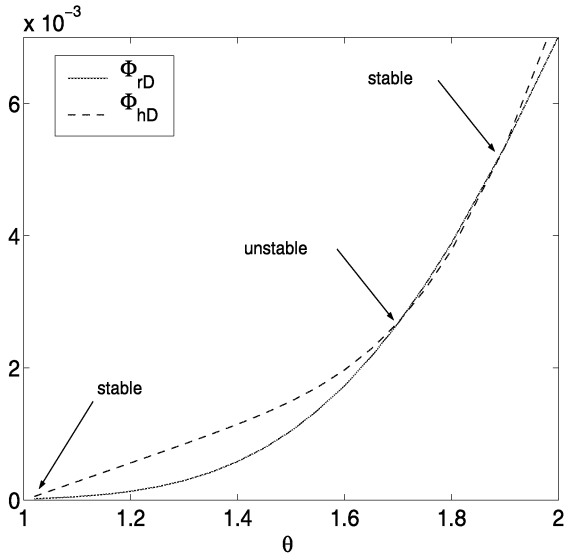

Figure 29: Nondimensional heat generation and loss rates versus nondimensional front temperature for convective type heat losses ($\tilde{h}/H$=0.3104 kW/m^3-K, injection velocity is 500 m/day). Existence of three steady states, two of which are stable.